Final Draft
of the original manuscript

Zhang, F.; Angelova, A.; Garamus, V.; Angelov, B.; Tu, S.; Kong, L.; Zhang, X.; Li, N.; Zou, A.:

Mitochondrial Voltage-Dependent Anion Channel 1–Hexokinase-II Complex-Targeted Strategy for Melanoma Inhibition Using Designed Multiblock Peptide Amphiphiles.

Mitochondrial Voltage-Dependent Anion Channel 1 (VDAC1)-Hexokinase-II (HK-II) Complex-Targeted Strategy for Melanoma Inhibition Using Designed Multi-Block Peptide Amphiphiles

Fan Zhang[a,b], Angelina Angelova[c], Vasil M. Garamus[d], Borislav Angelov[e], Shuyang Tu[f], Liangliang Kong[f], Xinlei Zhang[a], Na Li*[f], and Aihua Zou*[a,b]

[a] Shanghai Key Laboratory of Functional Materials Chemistry, School of Chemistry and Molecular Engineering, East China University of Science and Technology, Shanghai 200237, P. R. China, E-mail: aihuazou@shnu.edu.cn

[b] College of Chemistry and Materials Science, Shanghai Normal University, Shanghai 200234, P. R. China

[c] Université Paris-Saclay, CNRS, Institute Galien Paris-Saclay UMR8612, F-92290 Châtenay-Malabry, France

[d] Helmholtz-Zentrum Hereon, D-21502 Geesthacht, Germany

[e] Institute of Physics, ELI Beamlines, Academy of Sciences of the Czech Republic, Na Slovance 2, CZ-18221 Prague, Czech Republic

[f] National Facility for Protein Science in Shanghai, Shanghai Advanced Research Institute (Zhangjiang Laboratory), Chinese Academy of Sciences, Shanghai 201210, China, E-mail: nli@sibcb.ac.cn

ABSTRACT: Targeted therapies of melanoma are of urgent need considering the resistance of this aggressive type of cancer to chemotherapeutics. The VDAC1-HK-II complex is an emerging target for novel anti-cancer therapies based on induced mitochondria-mediated apoptosis. The low cell membrane permeability of the anti-cancer 12-mer peptide N-Ter (RDVFTKGYGFGL) derived from the N-terminal fragment of the VDAC1 protein impedes the intracellular targeting. Here, novel multi-block VDAC1-derived cationic amphiphilic peptides (referred to as Pal-N-Ter-TAT, pFL-N-Ter-TAT and Pal-pFL-N-Ter-TAT) are designed with self-assembly propensity and cell-penetrating properties. The created multi-block amphiphilic peptides of partial α-helical conformations formed nanoparticles of ellipsoid-like shapes and were characterized by enhanced cellular uptake. The amphiphilic peptides can target mitochondria and dissociate the VDAC1-HK-II complex at the outer mitochondrial membrane (OMM), which results in mitochondria-mediated apoptosis. The latter was associated with decrease of the mitochondrial membrane potential, Cytochrome c release, and changes of the expression levels of the apoptotic proteins in A375 melanoma cells. Importantly, the mitochondrial VDAC1-derived amphiphilic peptides have a comparable IC_{50} value for melanoma cells as the sorafenib small molecule drug, which has been previously used in clinical trials for melanoma. These results demonstrate the potential of the designed peptide constructs for efficient melanoma inhibition.

1

1. INTRODUCTION

Mitochondrial targeting receives increasing significance in the research for more efficient strategies for melanoma inhibition and treatment.[1-2] Mitochondria play a key role in regulating cancer cell survival and apoptosis.[3-5] Mitochondria-mediated apoptosis is provoked by changes in the mitochondrial membrane permeability, translocation of Cytochrome c from the mitochondrial intermembrane space to the cytosol, impaired cell metabolism, triggering of caspase activation and cell death signaling.[6-10] Mitochondria-mediated apoptosis can be activated also via targeting the B-cell lymphoma-2 (Bcl-2) family proteins using small molecules or peptidomimetic-based strategies,[11-13] hexokinase (HK) inhibitors,[14] VDAC1 targeting drugs,[15-19] growth factor withdrawal, increased production of reactive oxygen species (ROS), hypoxia or DNA damage.[20-21]

VDAC1, located at the outer mitochondrial membrane (OMM), is a multi-functional barrel protein.[17,22] It regulates mitochondrial energy metabolism by transporting various ions, active substances, and metabolites into and out of the mitochondria.[23] VDAC1 plays a key role in mitochondria-mediated apoptosis pathway via interactions with a variety of proteins with different functions (Figure 1).[23-24] VDAC1 protein-protein interaction inhibition offers emergent opportunities for development of more efficient anti-cancer therapies.

The N-terminal domain of VDAC1 plays a significant role in regulating cell metabolism and apoptosis.[23] Previous studies have suggested that the mobility of the N-terminal region (N-Ter) of VDAC1 is involved in channel gating, VDAC1 dimer formation,[25] and interaction with the anti-apoptotic proteins (*i.e.* HK).[14] N-Ter serves also as the interaction site for the apoptosis-regulating proteins of the Bcl-2 family (*i.e.* Bax, Bcl-2, and Bcl-xL).[26] VDAC1 binding to the

1 pro-apoptotic proteins (Bax) and oligomerization of VDAC1 into a channel pore triggers

2 Cytochrome c release, followed by apoptosis. At variance, the association of VDAC1 with anti-

3 apoptotic proteins (HK-II, Bcl-2 and Bcl-xL) protects cells against apoptosis.[27] Therefore,

4 approaches to prevent the anti-apoptotic activity of the anti-apoptotic proteins will be required to

5 induce cancer cell apoptosis.
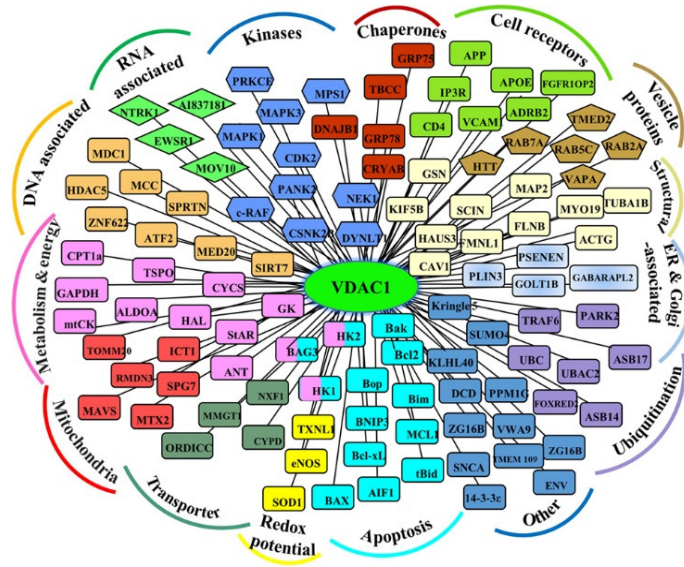
6

7 **Figure 1.** Mitochondrial VDAC1 protein-protein interactome, which can be explored for design

8 of novel anti-cancer peptide therapeutics (figure adapted from reference 24 under open-access

9 CC BY license with permission from Frontiers, 2017)[24].

10

11 Hexokinase-II (HK-II) bound to mitochondria is overexpressed in aggressive tumors, like

12 melanoma, as compared to its limited expression in normal tissues.[28-29] The interaction between

13 HK-II and VDAC1 is the molecular basis of the HK-II-mediated cell survival. Thus, dissociation

14 of HK-II from mitochondria and disruption of the VDAC1-HK-II interaction have emerged as a

15 very promising strategy for cancer treatment.[27] Anti-cancer agents that directly act on the

16 VDAC1-HK-II complexes have been studied in different cancer models.[17-19] Such apoptotic

1   compounds comprise enzymes that cleave the N-terminus of HK-II,[30] VDAC1-based peptides,[31]

2   hexokinase (HK) inhibitors (*e.g.* glucose-6-phosphate and its analogs)[32] as well as the antifungal

3   drugs clotrimazole[33] and bifonazole.[34] Recently, a novel HK-II protein-derived amphiphilic

4   peptide Pal-pHK-pKV with self-assembly and cell-penetrating properties has shown a potential

5   for targeting the VDAC1-HK-II complex and triggering lung cancer cell apoptosis with certain

6   selectivity for lung cancer *vs.* normal cells.[15]

7   The Shoshan-Barmatz's research group has intensively investigated the anti-cancer activity of

8   a series of N-terminal derived VDAC1-based peptides with different aminoacid sequence lengths

9   modified by the cell-penetrating peptide ANTP (RQIKIWFQNRRMKWKK).[23,35] The screening

10   studies with a short fragment RDVFTKGYGFGL (N-Ter) from VDAC1 have established the

11   anti-cancer activity of the VDAC1-based peptide and have revealed that the GYGFG

12   (GlyTyrGlyPheGly) sequence in the N-terminal of the protein is required for inducing cell

13   death.[35] Motivated by these reports on the anticancer activity of the N-Ter fragment of

14   VDAC1,[35] we have chosen the 12-amino acid peptide N-Ter as the template peptide for creation

15   of new anticancer agents with amphiphilic properties (Table 1). We hypothesize that the new

16   peptide derivatives may target the VDAC1-HK-II complex at the OMM of melanoma cells,

17   dissociate the HK-II protein from the mitochondrial membrane, and trigger mitochondrial-

18   mediated melanoma cell apoptosis.

19

20

21

1   **Table 1.** Conceived sequences of amphiphilic mitochondrial VDAC1-derived peptides

2   comprised by two, three or four building blocks and involving a fluorescent dansylglycine

3   residue.

Peptide	Sequence	MW	Charge at pH7
N-Ter[a]	RDVFTKGYGFGL	1360	+1
N-Ter-TAT[b]	RDVFTKGYGFGL-GRK(Dansylglycine)KRRQRRRPQ	3254	+8
Pal[c]-N-Ter-TAT	Pal-RDVFTKGYGFGL-GRK(Dansylglycine)KRRQRRRPQ	3492	+8
pFL[d]-N-Ter-TAT	FPWWWPFL-RDVFTKGYGFGL-GRK(Dansylglycine)KRRQRRRPQ	4414	+8
Pal-pFL-N-Ter-TAT	Pal-FPWWWPFL-RDVFTKGYGFGL-GRK(Dansylglycine)[e]KRRQRRRPQ	4652	+8

4

5   [a]N-Ter: N-terminal 12-mer peptide fragment of the VDAC1 protein with a propensity of

6   detaching the hexokinase (HK-II) from the OMM. [b]TAT: a positively charged cell penetrating

7   peptide (GRKKRRQRRRPQ) derived from the transactivation of transcription protein of the

8   human immunodeficiency virus (HIV). [c]Pal: a hydrophobic lipid chain of palmitic acid. [d]pFL: a

9   hydrophobic peptide fragment (FPWWWPFL) rich in tryptophan (W). [e]K(Dansylglycine): a

10 fluorescent amino acid residue located in the side chain of lysine (K).

11

12   In a preliminary study, we found that the N-Ter peptide has poor ability to internalize into

13 melanoma cancer cells, which is likely due to its low net charge and poor amphiphilicity. For this

14 reason, we propose here a self-assembly strategy exploiting designed amphiphilic peptides with

15 multiple building blocks. In recent years, synthetic peptides have found broad applications in

16 development of antibacterial materials,[36] biocatalyst,[37-39] and drug delivery systems.[40] However,

17 the clinical use of the peptide therapeutics has been hampered by their poor stability and short

18 half-life in the circulation. Strategies using amino acid substitution, cyclization, acetylation at the

19 N-terminus, amidation at the C-terminus of the peptide sequence, or loading into carriers,[41-45] are

expected to increase the peptide residence time at the target site. Self-assembly with amphiphilic

compounds has also been employed.[41-44,46] The self-assembly process is driven by various weak

interactions between the molecules including hydrogen bonding, electrostatic, hydrophobic, π-π

and van der Waals interactions.[45,47-49] Various types of nanostructures formed by amphiphilic

peptides, such as nanovesicles, nanofibers, and nanotubes, may affect the outcome of the

biological experiments with amphiphilic peptide.[46,50-53] Therefore, designing peptides with

specific structures and functions is an important trend towards advances in anti-cancer

nanomedicine.

Here, three-block amphiphilic peptides Pal-N-Ter-TAT and pFL-N-Ter-TAT were conceived

and custom synthesized by anchoring a 12-mer positively charged peptide (TAT) building block

at the C-terminus of the 12-mer N-Ter fragment. In this design, a hydrophobic palmitic acid

moiety or a short hydrophobic peptide (8-mer) building block (FPWWWPFL), rich in

tryptophan, was anchored at the N-Ter terminus. In order to further increase the amphiphilicity

of the construct, its self-assembly propensity, and interaction with lipid membranes, we created a

peptide of four building blocks. The peptide Pal-pFL-N-Ter-TAT (Table 1) was constructed by

modifying the pFL-N-Ter-TAT sequence with a hydrophobic palmitic acid moiety at the N-

terminus.

We hypothesize that the achieved hydrophobic-hydrophilic balance and structural features of

the obtained amino acid sequences may be crucial for the cytotoxicity of the designed

amphiphiles to melanoma cells. We consider that major challenges that limit the therapeutic

efficacy of peptide agents to cancer cells are the lack of amphiphilicity and the low α-helical

content in the peptide conformation, which is determinant for the weak peptide interactions with

the lipid membranes.[15]

1   The purpose of the present work is to investigate the self-assembly behavior of the new multi-

2   block amphiphilic peptides (Pal-N-Ter-TAT, pFL-N-Ter-TAT and Pal-pFL-N-Ter-TAT) (Table

3   1) and the targeting of the VDAC1-HK-II complex at the OMM in A375 cancer cells by these

4   amphiphilic peptides. Synchrotron Bio-SAXS, cryo-TEM imaging, and CD spectroscopy are

5   employed to characterize the structures of the self-assembled peptides. As the multi-block

6   amphiphilic peptides are designed to amplify cancer cell apoptosis based on disruption of the

7   VDAC1-HK-II contacts at the OMM, several bioassays are performed in order to assess the

8   mitochondria-mediated apoptosis process that may be triggered upon dissociation of the

9   VDAC1-HK-II complex.

10

11   **2. RESULTS AND DISCUSSION**

12   **2.1. Self-assembly behavior of novel mitochondrial VDAC1-based peptide amphiphiles**

13   The amino acid sequences of N-Ter and N-Ter-TAT (Table 1) did not exhibit amphiphilic

14   properties, owing to their hydrophobic/hydrophilic balance, and therefore did not form self-

15   assembled nano-objects in the studied concentration range from 0.1 to 1.5 mM. The self-

16   assembly behavior of the mitochondrial VDAC1-derived peptides Pal-N-Ter-TAT, pFL-N-Ter-

17   TAT and Pal-pFL-N-Ter-TAT into nanoscale objects was demonstrated by cryo-TEM

18   experiments at concentration 1.5 mM (Figure 2). The image contrast was relatively low due to

19   the lack of electron-rich atoms in the peptide molecules. Upon magnification, the cryo-TEM

20   images showed that Pal-N-Ter-TAT formed ellipsoid-like assemblies with an average length of

21   about 6 nm (Figure 2a). pFL-N-Ter-TAT formed ellipsoid-like assemblies with an average

22   length of about 8 nm (Figure 2b), whereas Pal-pFL-N-Ter-TAT formed ellipsoid-like assemblies

23   with an average length of about 12 nm (Figure 2c). The white dots in the center of other self-

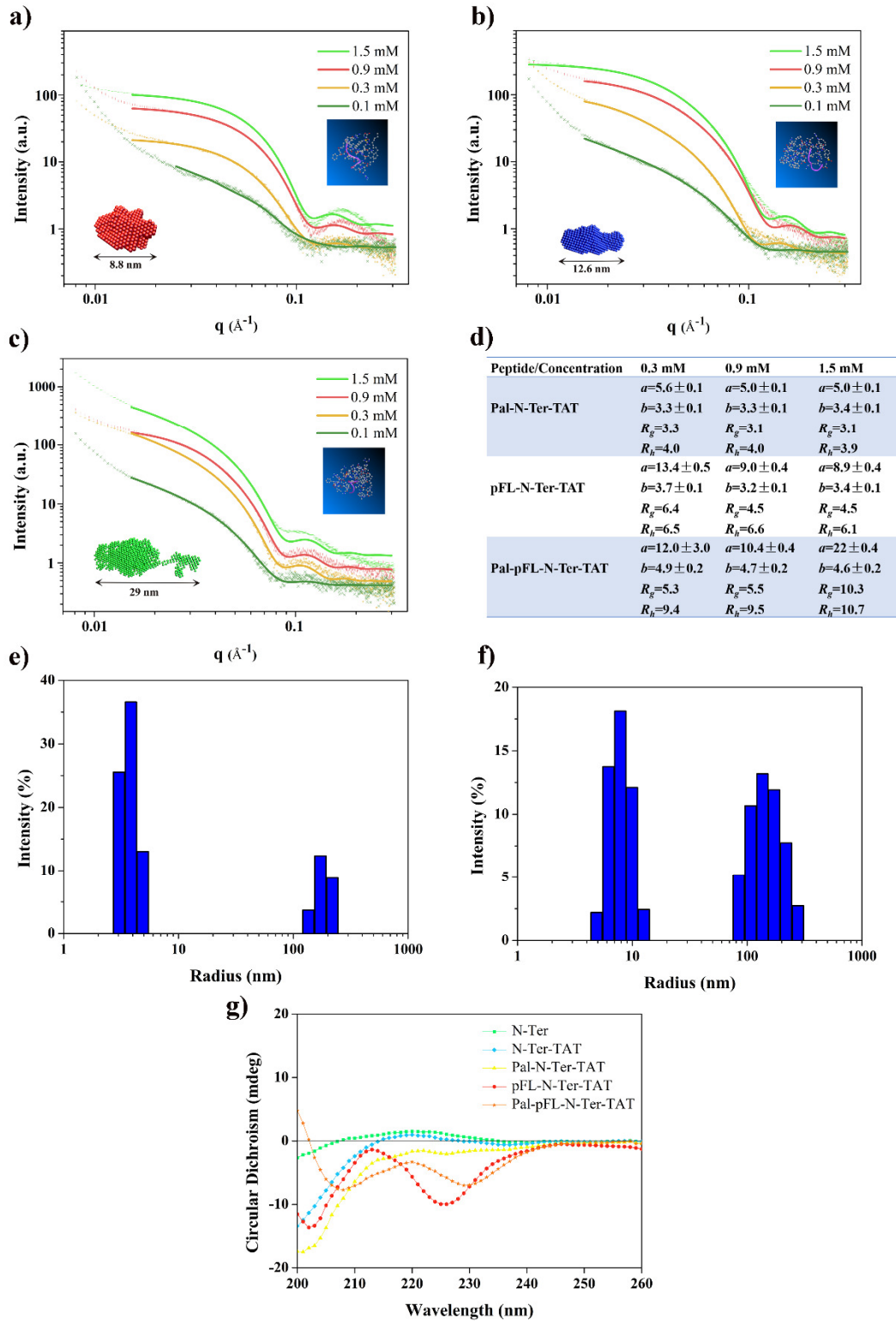assembled particles indicated the formation of hollow structures as shown by the arrow in Figure

2c.
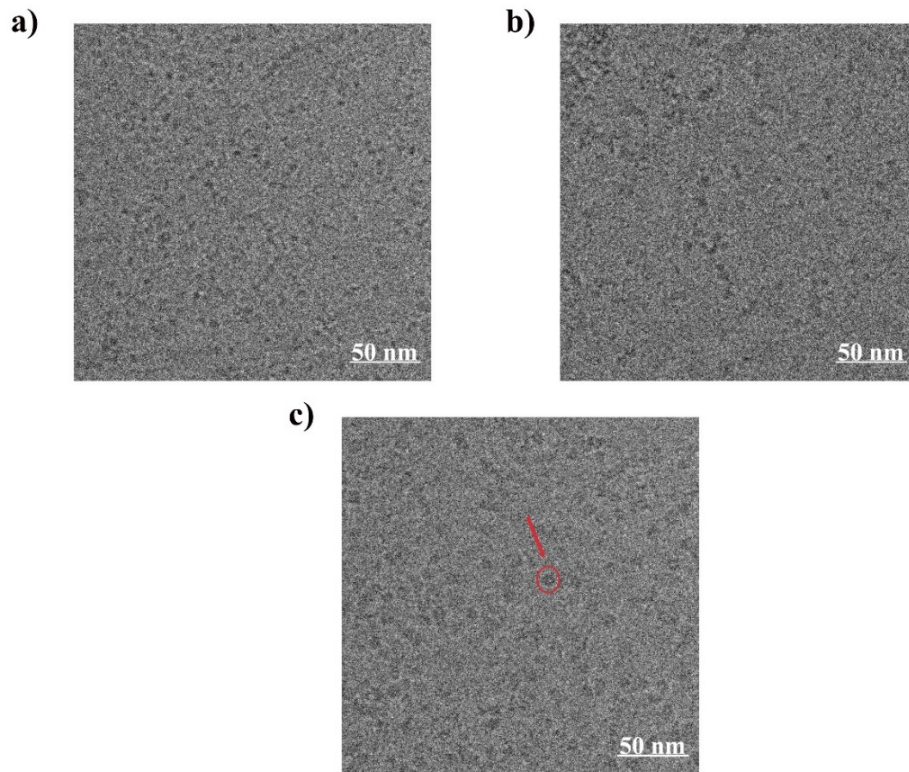
Figure 2. Cryo-TEM images of self-assembled nanoarchitectures formed by the designed mitochondrial VDAC1-derived amphiphilic peptides: a) Pal-N-Ter-TAT (1.5 mM); b) pFL-N-Ter-TAT (1.5 mM); c) Pal-pFL-N-Ter-TAT (1.5 mM). The majority of the assemblies displays ellipsoid-like shapes. Minor fractions illustrate formation of hollow structures.

The self-assembly behavior of the Pal-N-Ter-TAT, pFL-N-Ter-TAT and Pal-pFL-N-Ter-TAT peptides was further investigated by synchrotron BioSAXS as a function of the solution concentration (Figure 3a, 3b and 3c). All peptide assemblies showed scattering in the concentration range of 0.1–1.5 mM. This implies that the amphiphilic peptides are organized into supramolecular nano-objects.

1   The SAXS data did not show a plateau at the lowest q-vector range except for pFL-N-Ter-TAT

2   at 1.5 mM concentration (Figure 3b). The shape of the scattering curves and the significant

3   deviation from Guinier´s behavior $I(q) \sim \exp(-q^2 Rg^2/3)$, $q^2 Rg^2/3 \ll 1$ (where Rg is radius of

4   gyration of particle) is connected with the formation of larger structures. This points on the

5   presence of aggregated structures in the system, the sizes of which are outside the observation

6   window of the present SAXS experiments with a threshold $2\pi/q_{min}$ (~100 nm). Indeed, the

7   performed size measurements by quasi-elastic light scattering showed the presence of at least 2

8   populations of particles (Figure 3e and 3f). The small particles had a mean hydrodynamic radius

9   around 4-10 nm, whereas the fraction of larger particles was with a hydrodynamic radius about

10   100-200 nm.

11   The outer shapes of the obtained peptide assemblies were determined by the DAMMIN

12   method.[54] The objects are displayed in red (Figure 3a), blue (Figure 3b) and green (Figure 3c)

13   with indicated extended nanoscale dimensions determined from the *ab initio* modeling. This *ab*

14   *initio* analysis was performed for the highest concentration of the peptides as the fraction of the

15   compact small aggregates was predominant according to the particle size measurements.

Panel d) table:

Peptide/Concentration	0.3 mM	0.9 mM	1.5 mM
Pal-N-Ter-TAT	a=5.6±0.1 b=3.3±0.1 R_g=3.3 R_h=4.0	a=5.0±0.1 b=3.3±0.1 R_g=3.1 R_h=4.0	a=5.0±0.1 b=3.4±0.1 R_g=3.1 R_h=3.9
pFL-N-Ter-TAT	a=13.4±0.5 b=3.7±0.1 R_g=6.4 R_h=6.5	a=9.0±0.4 b=3.2±0.1 R_g=4.5 R_h=6.6	a=8.9±0.4 b=3.4±0.1 R_g=4.5 R_h=6.1
Pal-pFL-N-Ter-TAT	a=12.0±3.0 b=4.9±0.2 R_g=5.3 R_h=9.4	a=10.4±0.4 b=4.7±0.2 R_g=5.5 R_h=9.5	a=22±0.4 b=4.6±0.2 R_g=10.3 R_h=10.7

Figure 3. Synchrotron SAXS patterns of VDAC1-derived peptides in aqueous solutions a) Pal-N-Ter-TAT, b) pFL-N-Ter-TAT, and c) Pal-pFL-N-Ter-TAT at varying concentrations. The

insets show the shapes of the self-assembled peptide objects (red, blue and green) with the corresponding sizes obtained by the DAMMIN method as well as the monomer peptide modeling by molecular dynamics (insets with a blue background). d) Structural morphological parameters [semi axes of ellipsoids of revolution (*a, b, b*) and gyration radius (*Rg*)] of VDAC1-derived peptide assemblies deduced by BioSAXS analysis and hydrodynamic radii (*Rh*) for the small-particle population. The values are presented in [nm] units. Hydrodynamic radii of mitochondrial VDAC1-derived peptides assembly e) Pal-N-Ter-TAT and f) Pal-pFL-N-Ter-TAT determined at 0.9 mM solution concentration by quasi-elastic light scattering (DLS). g) Conventional CD spectra of 0.1 mM N-Ter, N-Ter-TAT, Pal-N-Ter-TAT, pFL-N-Ter-TAT and Pal-pFL-N-Ter-TAT in aqueous phase.

The analysis of the SAXS results indicated that the slope of the scattering intensities at the lowest q-vector range ($I(q) \sim q^{-\alpha}$) became smaller at increasing concentration of the peptides. This implies that the large aggregates become more compact at higher peptide concentrations. In the intermediate q-vector range, the scattering intensities corresponded to the presence of small aggregates, which entered in the observation window of the SAXS experiments (1-100 nm). The quantitative SAXS analysis was performed for the intermediate and large q-vector intervals, where the effect of coexisting bigger aggregates should be minimal. As a matter of fact, the shapes of all SAXS curves were similar in the concentration range 0.3–1.5 mM in the intermediate and large q-vector range (Figure 3a, 3b and 3c). This indicates that the shapes of the peptide aggregates negligibly change with the variation of the concentration under these experimental conditions. We performed fitting of the experimental scattering intensities by a model scattering from ellipsoids of rotation with semi axes *a, b, b*. The model considers excluded volume interactions among the aggregates for the interval of intermediate and large q-vector. It was not possible to completely reproduce the broad maximum around 0.15 Å^{-1} by the ellipsoid of rotation model. This was most probably due to contributions of ions around the surface of the

1   aggregates, which require transformation to few shell models and additional a prior information

2   for stable fitting procedure. The absence of maxima for pFL-N-Ter-TAT sample is connected

3   with length polydispersity of formed aggregates, which has not been taken into account in

4   modelling for better comparison with other samples.

5   The details of the formal analysis were analogous to those previously reported.[13] The fitting

6   parameters (semi axes of ellipsoid of revolution (*a, b, b*) and radius of gyration (*Rg*)) are given in

7   Figure 3d. The results showed that the length of the peptide aggregates increased upon dilution.

8   The peptide particles were more compact at higher concentrations, but this should be considered

9   with caution due to possible interference of the larger aggregates on the obtained parameters.

10   The ratio Rg/Rh gives the important information of shape, compactness, and structure of

11   hydration layer of the particles. It can be noted in Figure 3d that the ratio is always below 1 and

12   in some cases, it is above 0.774 (hard sphere ratio), which points on some elongated and/or

13   noncompacted structures. The first column in Figure 3d indicates that the shape of the Pal-N-

14   Ter-TAT assemblies is characterized by a ratio between the ellipsoid axes of around 1.5 at

15   concentration 1.5 mM. This result is confirmed by the obtained 3D model derived by the

16   DAMMIN method[54] (Figure 3a, red color object in inset). Considering the monomer mass of the

17   Pal-N-Ter-TAT peptide (3492.15 g mol^{-1}), it can be deduced from the scattering data that the

18   small aggregates contain about 22-23 monomer peptides. Both the gyration radius and the

19   hydrodynamic radius values support the conclusion for a compact structure of the aggregates.

20   The pFL-N-Ter-TAT assemblies, in which the peptide monomer mass is 4414.11 g mol^{-1}, is

21   slightly elongated in shape with an axis ratio slightly higher than 2. The aggregates are composed

22   of around 52-53 monomer peptides. The shape of the assembly is also confirmed by the 3D

23   model obtained by DAMMIN (Figure 3b, blue color object in inset).

1   The more hydrophobic Pal-pFL-N-Ter-TAT derivative (with a monomer peptide mass 4652.52

2   g mol^{-1}) appears to be strongly aggregated. The axis ratio is bigger than 2 (Figure 3d) and the

3   number of peptide molecules in one aggregate is estimated to be around 186-187 monomer

4   peptides based on the scattering data. The 3D model shows an elongated structure (Figure 3c,

5   green color object in inset), but the results should be considered with caution due to the

6   overlapping of the scattering signal from aggregates of different sizes.

7   The secondary structures of the mitochondrial VDAC1-derived peptides were investigated by

8   CD spectroscopy (Figure 3g). The secondary structure content of the peptides in 0.1 mM

9   solutions is shown in Table 2. The acquired data indicated that the helicity of N-Ter-TAT was

10   29.2%, whereas the helicity for Pal-N-Ter-TAT and pFL-N-Ter-TAT varies from 19.8% to

11   23.4%. Among the amphiphilic derivatives Pal-N-Ter-TAT, pFL-N-Ter-TAT and Pal-pFL-N-

12   Ter-TAT, the helicity for Pal-pFL-N-Ter-TAT was highest (29.8%). It may be expected that the

13   α-helical conformation has a higher propensity for interaction and insertion into lipid membranes

14   as well as for overcoming the biological membrane barriers.[15]

15

16   **2.2. Cytotoxicity and flow-cytometry cell apoptosis assays with mitochondrial VDAC1-**

17   **derived amphiphilic peptides**

18   The *in vitro* biological experiments with the novel multi-block peptides examined whether the

19   established amphiphilicity is a key factor affecting the cytotoxicity results. In the preliminary

20   work, we used the peptides Pal-N-Ter-TAT and Pal-pFL-N-Ter-TAT to respectively treat A549,

21   MCF-7 and A375 cells for 24 h. The results indicated that Pal-pFL-N-Ter-TAT displays

22   strongest anticancer activity in the three cancer cell lines and has the strongest toxicity to

23   melanoma A375 cells. Therefore, we have chosen the melanoma A375 cells as the research

1 objective in this work (Table S1). In addition, we studied whether the increased hydrophobicity

2 of the multi-block peptide constructs, for instance that of the Pal-pFL-N-Ter-TAT amphiphilic

3 peptide, may be advantageous for inhibition of melanoma cancer as compared to the small

4 molecule drug sorafenib,[55] which has been previously used in clinical trials for melanoma.

5   Human melanoma A375 cell viability was evaluated via MTT assays after treatment by

6 varying concentrations of N-Ter, N-Ter-TAT, Pal-N-Ter-TAT, pFL-N-Ter-TAT or Pal-pFL-N-

7 Ter-TAT peptides for 24 hours (Figure 4a). The results showed that N-Ter and N-Ter-TAT

8 peptides had negligible toxicity. At 50 μM concentration, cell viability after treatment by N-Ter

9 and N-Ter-TAT peptides were 94.08% and 87.00%, respectively. It can be concluded that the N-

10 Ter and N-Ter-TAT peptides have low amphiphilicity, owing to low hydrophobicity, and

11 therefore cannot easily penetrate into the cancer cells. In contrast, the anti-proliferative activity

12 of the amphiphilic peptides is notably enhanced.

13   The half maximal inhibitory concentration (IC_{50}) values of Pal-N-Ter-TAT, pFL-N-Ter-TAT

14 and Pal-pFL-N-Ter-TAT peptides for A375 cancer cells after 24 h treatment were determined to

15 be 15.2±0.7 μM, 11.1±0.1 μM and 5.5±1.1 μM. Therefore, the amphiphilic amino acid sequences

16 appear to interact more strongly with the cellular membranes. The fact that the Pal-pFL-N-Ter-

17 TAT conjugate shows an improved anti-cancer effect as compared to sorafenib (IC_{50}=7.0±0.2

18 μM), which is used in clinical trials for melanoma, suggests that the new peptide has a greater

19 potential for melanoma inhibition.
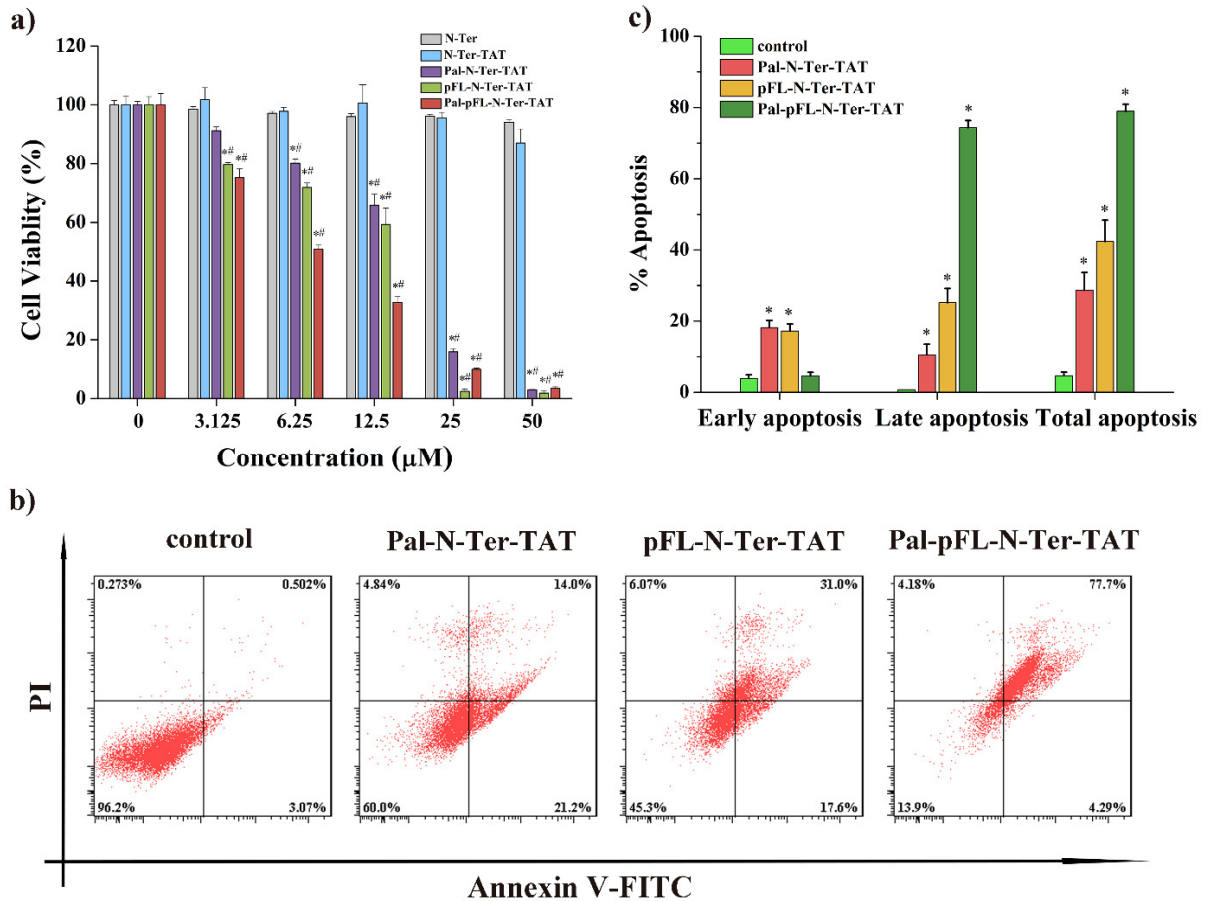
Figure 4. a) Determination of cellular viability with MTT assays. Cancer A375 cells were treated with various concentrations of N-Ter, N-Ter-TAT, Pal-N-Ter-TAT, pFL-N-Ter-TAT or Pal-pFL-N-Ter-TAT peptides for 24 h. Untreated cells were measured as a control. *P＜0.01 compared to N-Ter and #P＜0.01 compared to N-Ter-TAT. Data were presented as mean ± SD (n=3). Determination of cellular apoptosis of A375 cells that were treated with 12.5 μM Pal-N-Ter-TAT, pFL-N-Ter-TAT or Pal-pFL-N-Ter-TAT peptides for 4 h. b) FACS analysis after Annexin V-FITC/PI staining. c) A summary of the incidence of early apoptosis, late apoptosis and total apoptosis in A375 cancer cells. *P < 0.01 compared with controls. Data were presented as mean ± SD (n = 3).

The IC_{50} values of the mitochondrial VDAC1-derived peptides, determined from the cytotoxicity assays with A375 cancer cells, are compared in Table 2. The results indicated that

16

1   the amphiphilic peptides Pal-N-Ter-TAT, pFL-N-Ter-TAT and Pal-pFL-N-Ter-TAT displayed

2   enhanced A375 cell growth inhibition as compared to the non-amphiphilic peptide N-Ter-TAT.

3   Among the amphiphilic peptides, Pal-pFL-N-Ter-TAT exhibited the most potent anti-cancer

4   effect and this outcome was consistent with the increased α-helical content (Table 2). These

5   results imply that amphiphilicity and α-helical structure play an important role for the peptide

6   activity towards melanoma cell growth inhibition. A correlation can be suggested between the

7   cytotoxicity and the designed molecular structures composed of multiple (hydrophobic and

8   hydrophilic) building blocks (Table 1).

9

10 **Table 2.** Correlation between the designed multi-block peptide molecular structures and the

11 cytotoxicity against melanoma cancer cells. The α-helicity content and the IC_{50} values obtained

12 from cytotoxicity assays are indicated for every peptide.

Peptides	Helicity (%)	IC_{50} (μM)
N-Ter	8.1	>50.0
N-Ter-TAT	29.2	>50.0
Pal-N-Ter-TAT	19.8	15.2±0.7
pFL-N-Ter-TAT	23.4	11.1±0.1
Pal-pFL-N-Ter-TAT	29.8	5.5±1.1
Sorafenib	-	7.0±0.2

13

14 An Annexin V-FITC/PI apoptosis detection kit was used to examine by flow cytometry the

15 ability of Pal-N-Ter-TAT, pFL-N-Ter-TAT and Pal-pFL-N-Ter-TAT peptides to induce

16 melanoma cell apoptosis (Figure 4b and 4c). The A375 cells were exposure to 12.5 μM Pal-N-

17 Ter-TAT, pFL-N-Ter-TAT or Pal-pFL-N-Ter-TAT peptide derivatives, respectively, for 4 h. The

1 results indicated that the total apoptosis for A375 cells treated with Pal-N-Ter-TAT and pFL-N-

2 Ter-TAT were 35.2% and 48.6%, respectively, whereas the total apoptosis for cells treated with

3 Pal-pFL-N-Ter-TAT was 81.99%. These data demonstrate that Pal-pFL-N-Ter-TAT is

4 significantly more efficient to induce melanoma cell apoptosis. In all cases, the apoptosis

5 pathway is determinant for the cancer cell death triggered by the Pal-N-Ter-TAT, pFL-N-Ter-

6 TAT and Pal-pFL-N-Ter-TAT constructs.

7   The flow cytometry results revealed that the amphiphilic Pal-pFL-N-Ter-TAT peptides are

8 characterized by a highest capacity to induce dissociation of HK-II from VDAC1 at the OMM

9 and trigger melanoma A375 cancer cell death. This opens new opportunities for the development

10 of mitochondria-targeting peptide amphiphiles in anti-cancer strategies.

11

12 **2.3. Intracellular localization of mitochondrial VDAC1-derived amphiphilic peptides in**

13 **melanoma cells followed by detachment of mitochondria-bound HK-II**

14   The intracellular localization of the novel amphiphilic peptides upon uptake by A375 cancer

15 cells was investigated by confocal fluorescence microscopy imaging. As noted above, the

16 investigated peptide constructs contain the fluorescent dansylglycine residue (Table 1). The

17 detected fluorescence of the internalized peptides is displayed in blue color in Figure 5a. The

18 A375 cells were exposed to 12.5 μM Pal-N-Ter-TAT, pFL-N-Ter-TAT or Pal-pFL-N-Ter-TAT

19 for 4 h. The fluorescence signals from the A375 cells treated with Pal-N-Ter-TAT were weaker

20 as compared to those observed with pFL-N-Ter-TAT and Pal-pFL-N-Ter-TAT. This may be due

21 to insufficient uptake of Pal-N-Ter-TAT. In contrast, intensive fluorescence signals were

22 recorded with A375 cancer cells incubated with pFL-N-Ter-TAT and Pal-pFL-N-Ter-TAT

23 peptides, which are characterized by increased cellular uptake. These results were consistent with

1 the flow cytometry data for the cellular uptake of the dansylglycine-labelled peptides (Figure

2 S1). Thus, the fact that the observed intracellular uptake is related to the amphiphilic structure of

3 the peptide conjugates appears to be in agreement with the flow cytometry results.
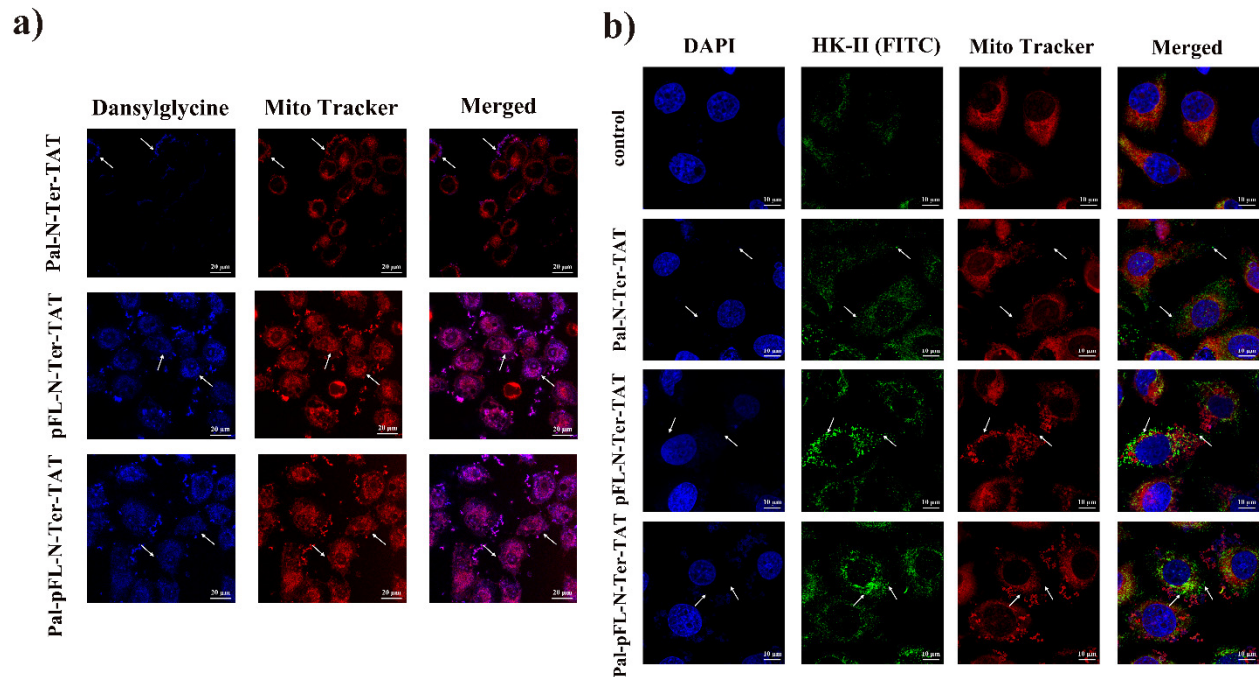
4
5 **Figure 5.** a) Confocal microscopy study of intracellular localization of the investigated peptides.

6 The A375 cells were incubated with 12.5 µM Pal-N-Ter-TAT, pFL-N-Ter-TAT or Pal-pFL-N-

7 Ter-TAT for 4 h. The blue color indicates the fluorescence due to the uptake of the

8 dansylglycine-labeled peptide. The red color is associated with the mitochondrial staining by 100

9 nM MitoTracker Deep Red dye. The arrows indicate the co-localization established by the

10 merged images. b) Confocal microscopy study of detachment of mitochondria-bound HK-II by

11 immunofluorescence. The A375 cells were incubated with 12.5 µM Pal-N-Ter-TAT, pFL-N-Ter-

12 TAT or Pal-pFL-N-Ter-TAT for 4 h. The blue color corresponds to the location of the cell

13 nucleus. The green color is associated with HK-II by immunostaining using anti-HK-II antibody.

14 The red color shows the fluorescence of MitoTracker Deep Red dye of stained mitochondria.

15 The arrows indicate HK-II dissociated from mitochondria.

16

1   Figure 5a (merged images) demonstrates the co-localization between the mitochondria of the

2   treated melanoma cells and the amphiphilic peptides internalized in the cells. The comparison of

3   the images evidenced the distribution of the dansylglycine-labeled fluorescent peptides (blue

4   color) and the fluorescence location of the mitochondria-targeting MitoTracker dye (red color).

5   The obtained merged confocal fluorescence images confirmed that mitochondrial membranes are

6   indeed the target site for the studied VDAC1-derived amphiphilic peptides, which was further

7   demonstrated by the results of cell co-localization of peptide-treated A375 cells for 2 h (Figure

8   S2).

9   The detachment of mitochondria-bound HK-II was studied by confocal fluorescence

10   microscopy imaging (Figure 5b). The A375 cells were incubated with 12.5 μM Pal-N-Ter-TAT,

11   pFL-N-Ter-TAT or Pal-pFL-N-Ter-TAT for 4 h. The co-localization of green [HK-II (FITC)]

12   and red fluorescence (MitoTracker) of control cells indicated the mitochondrial distribution of

13   HK-II. In contrast, part of the green fluorescence signal of peptide-treated cells essentially did

14   not co-localize with the red fluorescence signals, pointing to the detachment of HK-II from

15   mitochondria. Moreover, mitochondrial blebbing in peptide-treated A375 cells revealed the

16   occurrence of cell apoptosis.

17   Therefore, it can be suggested that the new VDAC1-derived peptides target the mitochondria,

18   detach HK-II from the mitochondria, and trigger the A375 cells apoptosis. The mitochondria-

19   mediated A375 cancer cells apoptosis is further studied in the next section.

20

21   **2.4. Mitochondrial membrane potential changes, immunofluorescence and western blot**

22   **analysis evidencing the mitochondria-mediated A375 cancer cell apoptosis triggered by**

23   **VDAC1-derived amphiphilic peptides**

1   Fluorescence microscopy with JC-1 staining was used to detect the mitochondrial membrane

2   potential changes of A375 cells treated by peptide constructs (Figure 6a). The decrease of the

3   mitochondrial membrane potential is a marker of early apoptosis. In healthy mitochondria, the

4   JC-1 dye can form aggregates generating red fluorescence. At variance, the JC-1 dye is in a

5   monomeric form, generating green fluorescence in unhealthy cells, in which the mitochondria-

6   mediated apoptosis pathway is triggered. Compared with a control group, the A375 cells

7   incubated with 12.5 µM Pal-N-Ter-TAT, pFL-N-Ter-TAT and Pal-pFL-N-Ter-TAT for 4 h

8   showed increased green fluorescence and decreased red fluorescence, which indicates the

9   decrease of the mitochondrial membrane potential. These effects reveal that the mitochondria-

10   mediated apoptosis is initiated. The red fluorescence intensity of the Pal-N-Ter-TAT-treated

11   group was comparable with the red fluorescence intensity of the pFL-N-Ter-TAT-treated group.

12   The red fluorescence intensity of the Pal-pFL-N-Ter-TAT-treated group was the weakest, which

13   agrees with the flow cytometry results.

14

15
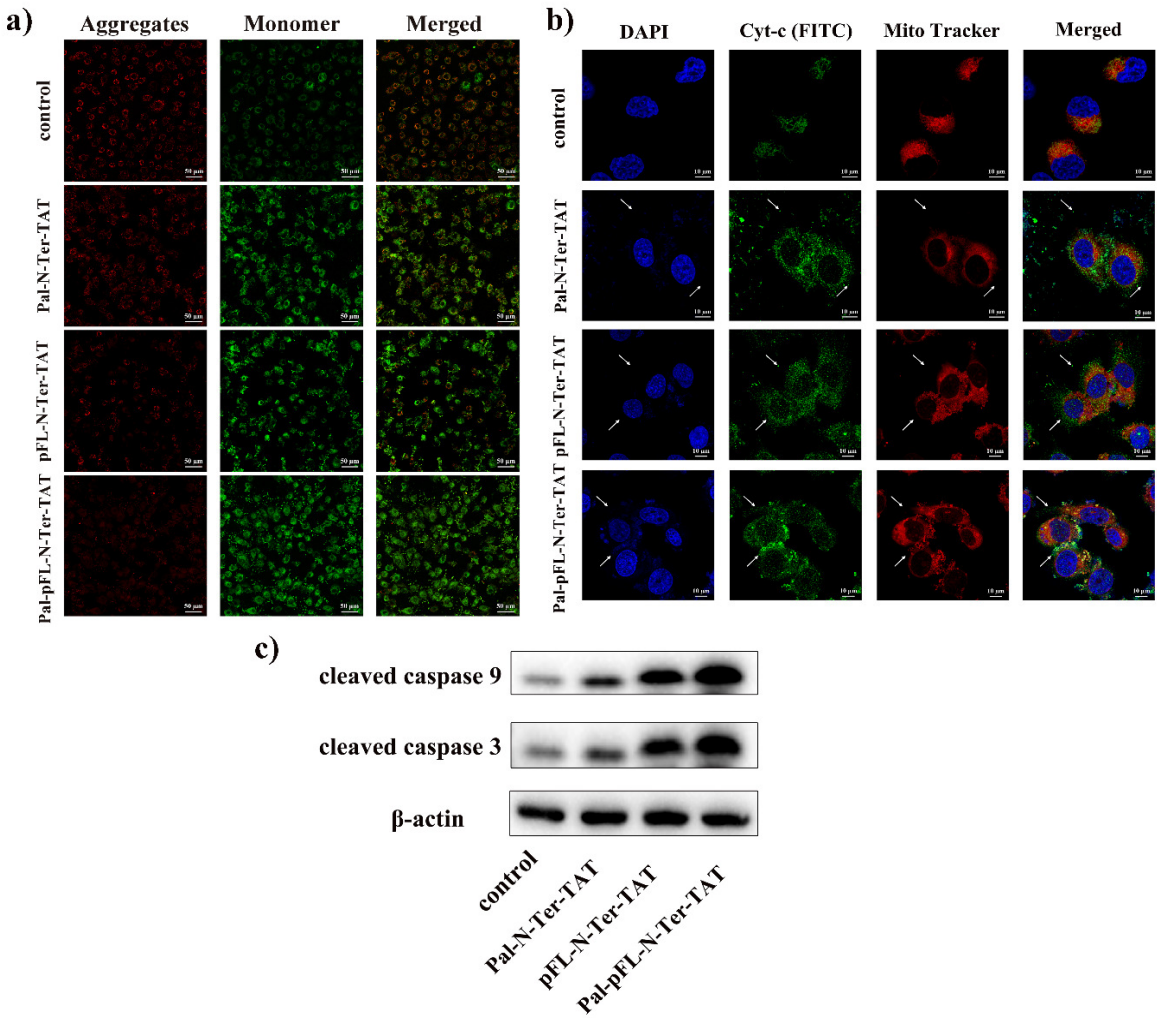
Figure 6. a) Changes in the mitochondrial membrane potential of A375 cells that were treated with 12.5 μM Pal-N-Ter-TAT, pFL-N-Ter-TAT or Pal-pFL-N-Ter-TAT amphiphilic peptides for 4 h (fluorescence microcopy detection by the JC-1 kit). Mitochondria-mediated apoptosis of melanoma A375 cells incubated with 12.5 μM Pal-N-Ter-TAT, pFL-N-Ter-TAT or Pal-pFL-N-Ter-TAT evidenced by immunofluorescence and Western blot analysis. b) Detection of Cytochrome c release in A375 cells treated by peptides for 4 h. The blue color indicates the location of the cell nucleus. The green color is associated with Cytochrome c by immunostaining using an anti-Cytochrome c antibody. The red color shows the fluorescence of MitoTracker Deep Red dye in the stained mitochondria. The arrows indicate Cytochrome c release. c) Changes in the expression levels of apoptosis-associated proteins in A375 cells that were treated by peptides for 24 h.

Cytochrome c release was investigated via immunofluorescence experiments. A375 cells were incubated with 12.5 μM Pal-N-Ter-TAT, pFL-N-Ter-TAT or Pal-pFL-N-Ter-TAT for 4 h. Representative images of control cells showed co-localization of most green fluorescence signals and red fluorescence signals, suggesting mitochondrial distribution of Cytochrome c. In peptide-treated cells, part of the green fluorescence signals did not co-localize with the red fluorescence signals, pointing to the release of Cytochrome c (Figure 6b).

The expression levels of apoptosis-associated proteins, as evidence for mitochondria-mediated apoptosis, were determined using Western blot technology (Figure 6c). Cellular proteins were extracted from melanoma A375 cells treated with 12.5 μM Pal-N-Ter-TAT, pFL-N-Ter-TAT or Pal-pFL-N-Ter-TAT for 24 h using Column Tissue and Cell Protein Extraction Kits. The results in Figure 6c showed that the expression levels of cleaved caspase 3 and cleaved caspase 9 proteins were significantly upregulated as compared to a control group. This reveals that mitochondria-mediated apoptosis is indeed triggered. For pFL-N-Ter-TAT, the expression levels of three apoptosis-associated proteins were higher in the treated group than for the Pal-N-Ter-TAT-treated group. However, the expression levels of the three apoptosis-associated proteins were highest for the melanoma treatment by Pal-pFL-N-Ter-TAT. These results agree with the flow cytometry results and the other biological tests.

The decrease of the mitochondrial membrane potential, Cytochrome c release, and the increased expression levels of cleaved caspase 3 and cleaved caspase 9 proteins in A375 cells treated with amphiphilic peptides prove that the cancer cell death is induced via mitochondria-mediated apoptosis pathway. Evidently, the Pal-pFL-N-Ter-TAT multi-block peptide has an enhanced activity in inducing mitochondria-mediated apoptosis of melanoma

1 cells.
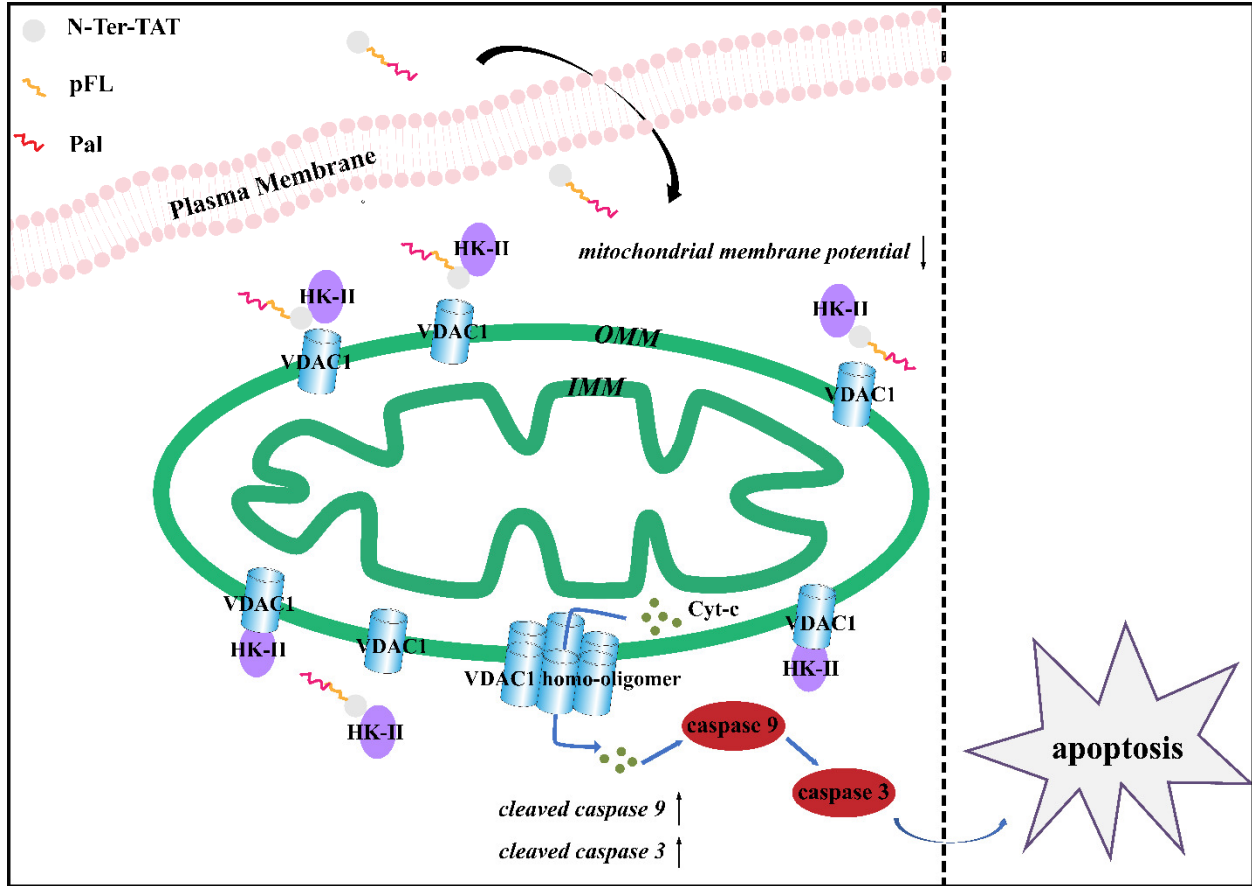
Figure 7. Proposed model of mitochondrial VDAC1-derived amphiphilic peptide action. Once in the cytosol, Pal-pFL-N-Ter-TAT peptides target the mitochondrial membrane, where they can detach HK-II from VDAC1 at the outer mitochondrial membrane. The disruption of the VDAC1-HK-II interaction leads to the decrease of the mitochondrial membrane potential, Cytochrome c release and increased expression levels of cleaved caspase 3 and cleaved caspase 9 proteins, and finally to apoptosis. The mechanism of action of the Pal-N-Ter-TAT and pFL-N-Ter-TAT peptides is likely the same as the Pal-pFL-N-Ter-TAT peptide.

In summary, the mitochondrial VDAC1-derived amphiphilic peptides Pal-N-Ter-TAT, pFL-N-Ter-TAT and Pal-pFL-N-Ter-TAT target the cancer cell mitochondrial membrane and dissociate

HK-II from VDAC1 at the OMM (Figure 7). Inducing the mitochondria-mediated apoptosis pathway and the disruption of the VDAC1-HK-II interaction results in the decrease of the mitochondrial membrane potential, release of Cytochrome c and increased expression levels of cleaved caspase 3 and cleaved caspase 9 proteins. Taken together, Pal-N-Ter-TAT, pFL-N-Ter-TAT and Pal-pFL-N-Ter-TAT are novel amphiphilic CPP with potent anticancer properties. Further to the published work on the VDAC1 protein and VDAC1-derived peptides,[56-XX] these amphiphilic constructs may serve for development of alternative therapeutic tools.

3. CONCLUSIONS

VDAC1 is overexpressed in many cancer types including human melanoma. In this study, we designed novel mitochondrial VDAC1-derived peptide amphiphiles for melanoma inhibition via minimization of the self-defense mechanisms of the cancer cells. Induction of apoptosis was achieved through protein–protein interaction inhibition using rationally designed amphiphilic peptide structures. Pal-N-Ter-TAT, pFL-N-Ter-TAT and Pal-pFL-N-Ter-TAT derivatives were created from a 12-mer fragment of the N-terminal of VDAC1 (N-Ter), which was anchored to two kinds of hydrophobic building blocks and a positively charged cell-penetrating peptide TAT. The outcome of the peptide amphiphile design was investigated by high resolution structural methods, which revealed supramolecular peptide self-assembly into ellipsoid-like aggregates with nanometric dimensions. The secondary structures of the novel peptide amphiphiles involved partial α-helical conformations. Notably, Pal-pFL-N-Ter-TAT displayed a higher helicity, which implied stronger interaction with the lipid membranes. It is suggested that the amphiphilicity is essential for the cytotoxicity to melanoma cells. The obtained peptide amphiphiles had a lower IC_{50} value in experiments on A375 cancer cell inhibition as compared to the soluble N-Ter and

N-Ter-TAT peptides. The IC_{50} value of the Pal-pFL-N-Ter-TAT peptide was found to be lower than that of sorafenib, which has been tested in clinical trials for melanoma. All Pal-N-Ter-TAT, pFL-N-Ter-TAT and Pal-pFL-N-Ter-TAT constructs were found to (i) co-localize with mitochondria, (ii) detach HK-II from mitochondria, and (iii) induce mitochondria-mediated A375 cancer cell apoptosis. Among them, the Pal-pFL-N-Ter-TAT peptide has shown an increased bioactivity against melanoma cells as evidenced by the significantly upregulated levels of the apoptosis-associated proteins. It is concluded that the designed amphiphilic peptide structure with two hydrophobic building blocks and a positively charged TAT anchor is determinant for the efficacy of the peptide internalization and the exerted activity at the OMM target site in melanoma cells. Therefore, the Pal-pFL-N-Ter-TAT peptide amphiphile appear to be promising for the development of more efficient anti-cancer therapeutic strategies based on targeting of the mitochondrial VDAC1-HK-II complex.

4. MATERIALS AND METHODS

4.1. Reagents and materials. The designed peptides sequences (shown in Table 1) were custom synthesized by Nanjing Peptide Biotech Ltd (China). Dimethyl sulfoxide (DMSO) was purchased from Aladdin Chemical Reagent Co. Ltd (China). Dulbecco's modified Eagle's medium (DMEM), Fetal Bovine Serum (FBS) and 0.25% trypsin–EDTA were purchased from Gibco (USA). An annexin V-FITC/PI apoptosis detection kit was purchased from Boster Biological Technology Co., Ltd (China). 3-(4,5-Dimethylthiazol-2-yl)-2,5-diphenyltetrazolium bromide (MTT) kits, JC-1 kits and MitoTracker Deep Red FM were purchased from MKBio (China). Sorafenib was purchased from CSNpharm (USA). Caspase 3 rabbit pAb and caspase 9 rabbit pAb, β-actin rabbit mAb, HRP goat anti-rabbit IgG (H+L) and FITC goat anti-Rabbit IgG

(H+L) were purchased from ABclonal (China). HK-II rabbit pAb and Cytochrome c rabbit pAb were purchased from Proteintech Group, Inc Rosement, IL 60018 (USA). Antifade solution (DAPI) was purchased from meilun Biotechnology Co., Ltd (China). Omni-PAGETM Hepes-Tris Gels, PVDF membranes and Omni-ECLTM Femto Light Chemiluminexscence Kit were purchased from EpiZyme (China).

4.2. Custom peptide synthesis. The studied peptides were synthesized by Standard Fmoc Solid Phase Techniques. Reverse-phase high performance liquid chromatography (Hanbon, NP7005C, China) with a Kromasil C18 column was used to isolate and purity the crude peptides. Mobile phases of HPLC were consist of solvent A (0.1% TFA in acetonitrile) and solvent B (0.1% TFA in water) and a liner gradient was from 20% to 100% solvent A. Purity and mass were respectively determined by high performance liquid chromatography -mass spectrometry (SHIMADZU, LCMS-2020, Japan). The purity of all peptides was $>$ 98% and peptide lyophilized powder was stored at -20 ℃ until need.

4.3. Small-angle X-ray scattering (SAXS) experiments. SAXS experiments were performed at the BL19U2 beamline of the Shanghai Synchrotron Radiation Facility (Shanghai, China). In order to reduce radiation damage, samples were loaded into flow cells made of cylindrical quartz capillary. The X-ray beam wavelength was 1.033 Å. A Pilatus 1M detector (DECTRIS Ltd) was employed to measure the intensity of X-ray scattering. A beam size of 0.40 mm × 0.15 mm was adjusted to pass through the center of the capillary in every measurement. The detection range of the scattering vector q was from 0.007 to 0.35 Å. The exposure time of each sample was 1 s. The software BioXTAS RAW was used to average the similar data, then subtract the background, and finally convert the two-dimensional scattering images into a one-dimensional SAXS curve. The *ab initio* shapes were determined using DAMMIN.

1   **4.4. Cryogenic transmission electron microscopy (cryo-TEM).** Cryo-TEM experiments

2   were performed at National Center for Protein Science Shanghai (Shanghai, China). peptide

3   samples (3 µL) were placed on a carbon-coated holey copper grid with a diameter of 3 mm that

4   had been hydrophilized, blotted with a filter paper leaving a thin liquid film, instantly immersion

5   into liquid ethane at -180 ℃ to vitrified and cooled at liquid nitrogen. The sample copper grid

6   was transferred into a Tecnai G2 F20 transmission electron microscopy which was operated at an

7   acceleration voltage of 200 kv. The structural image of the sample was taken with a 4 k × 4 k

8   CCD camera system.

9   **4.5. Circular dichroism (CD) analysis.** CD spectra of all peptides (0.1 mM) were measured

10   at room temperature on a Jasco J-810 spectrometer (Jasco Co., Japan) employing a quartz cell

11   with a pathlength of 1 mm. The spectra were recorded in the UV range of 190-250 nm at a scan

12   rate of 60 nm min^{-1}. The measurements were performed three times. The content of various

13   secondary structures of the peptide in PBS buffer was calculated by the BESTSEL tool

14   (http://bestsel.elte.hu/index.php).

15   **4.6. Cell culture growth.** The human Melanoma A375 cells were cultured in DMEM medium

16   containing 10% (v/v) fetal bovine serum, penicillin (100 U mL^{-1}), streptomycin (100 g mL^{-1}) in a

17   sterile incubator at 37 °C, in 5% CO_2 saturated humidity atmosphere.

18   **4.7. Cytotoxicity assays.** Cell viability was determined via MTT assay. A375 cells in

19   logarithmic growth phase were seeded in 96-well plates at a cell density of 5×10^4 cells per well.

20   Cells were incubated for 24 h to grow fully adherent. After removing the medium and washing

21   the cells with PBS, DMEM medium that contained N-Ter, N-Ter-TAT, Pal-N-Ter-TAT, pFL-N-

22   Ter-TAT or Pal-pFL-N-Ter-TAT peptide at concentrations of 0, 3.125, 6.25, 12.5, 25, 50 µM

23   were added to the wells (100 µL per well). The cells were incubated at 37 ℃ for 24 h. Then,

1 MTT solution (5 mg mL^{-1}, 10 µL) was added to each well and incubate for 4 h at 37 ℃. The

2 solution was removed and DMSO (100 µL) was added to each well. OD values were measured at

3 492 nm and 630 nm. The formula:

4 Viability (%) = (Mean OD value of treatment group-blank)/(Mean OD value of control group-

5 blank) × 100%

6 was used to calculate cell viability. The IC$_{50}$ values were analyzed by GraphPad Prism 7

7 software.

8 **4.8. Cell apoptosis assays.** The annexin V-FITC/PI apoptosis detection kit was used to detect

9 the rate of apoptosis cells in accordance with the manufacturer's protocol on a BD LSRFortessa

10 Flow Cytometer (BD Biosciences, USA). Briefly, A375 cells were seeded in a 6-well plate at a

11 density of 1×10^5 cells per well for 24 h followed by incubation with Pal-N-Ter-TAT, pFL-N-

12 Ter-TAT or Pal-pFL-N-Ter-TAT peptide (12.5 µM) for 4 h. The cells were detached with the

13 EDTA-free trypsin solution, centrifugated at 1000 rpm for 5 min, washed twice with cold PBS

14 and resuspended in 1×binding buffer (195 µL). Then, in the dark, the cells were incubated with

15 annexin V-FITC (5 µL) for 15 min and washed with 1×binding buffer (200 µL). The cells were

16 collected, resuspended in 1×binding buffer (190 µL) and incubated with PI (10 µL) in the dark.

17 In order to avoid fluorescence decay, all samples were tested within 4 h. The fluorescence

18 measurements were conducted at excitation wavelengths of 488 nm and 561 nm and emission

19 wavelengths of 530 nm and 575 nm for the FITC-conjugated annexin V and PI, respectively.

20 **4.9. Intracellular co-localization study.** The intra-cellular distribution of the Pal-N-Ter-TAT,

21 pFL-N-Ter-TAT and Pal-pFL-N-Ter-TAT peptides were viewed under a Zeiss LSM 710

22 confocal laser scanning microscope (Zeiss, Germany). Briefly, the A375 cells were seeded into a

23 20 mm glass bottom dish at a density of 4×10^4 cells per cm^2 for 24 h, incubated with Pal-N-Ter-

TAT, pFL-N-Ter-TAT or Pal-pFL-N-Ter-TAT peptide (12.5 µM) for 4 h. Thereafter, in order to stain the mitochondria, the cells were treated with 100 nM MitoTracker Deep Red FM for 25 min at 37 ℃. Finally, the cells were fixed with 4% paraformaldehyde for 20 min at 37 ℃. The fluorescence measurements were conducted at excitation wavelengths of 405 nm and 633 nm and emission wavelengths of 451 nm and 697 nm for the dansylglycine-conjugated peptides and MitoTracker Deep Red FM, respectively. ZEN software was used to process image.

4.10. Detachment of mitochondria-bound HK-II and Cytochrome c release assay by immunofluorescence experiment. Mitochondria-bound HK-II detachment and Cytochrome c release were investigated on Zeiss LSM 710 confocal laser scanning microscope (Zeiss, Germany). Briefly, the A375 cells were seeded into a 96-well glass bottom plates for 24 h, followed by incubation with the Pal-N-Ter-TAT, pFL-N-Ter-TAT or Pal-pFL-N-Ter-TAT peptides (12.5 µM, 4 h). Then, They were washed with PBS, paraformaldehyde-fixed (4%, 10 min), washed with PBS, permeabilized with 0.1% Triton X-100 in 3% BSA (30 min), incubated with anti-HK-II antibodies or anti-Cyt-c antibodies (1:200, 2 h), washed with PBS-0.5% Triton X-100, and then incubated with secondary FITC-conjugated anti-rabbit antibodies (1:200, 30 min), washed with PBS-0.5% Triton X-100 and stained with MitoTracker Deep Red FM (45 min). Finally, the cells were washed with PBS, treated with antifade solution (DAPI). The fluorescence measurements were conducted at excitation wavelength of 405 nm and emission wavelength of 451 nm for the DAPI. ZEN software was used to process image.

4.11. Measurement of the mitochondrial membrane potential. The mitochondrial membrane potential was measured by JC-1 kit according to manufacturer's instructions. Briefly, the A375 cells were seeded into a 20 mm glass bottom dish at a density of 4×10^4 cells per cm^2 for 24 h, treated with Pal-N-Ter-TAT, pFL-N-Ter-TAT or Pal-pFL-N-Ter-TAT peptide (12.5

1 µM) for 4 h. The cells were washed twice with cold PBS and incubated with JC-1 working

2 buffer at 37 °C for 20 min in the dark. Thereafter, the cells were washed twice with JC-1 staining

3 buffer and observed under a Zeiss LSM 710 confocal laser scanning microscope (Zeiss,

4 Germany) (magnification, x20). JC-1 monomers and JC-1 aggregates were excited at 488 nm

5 and 561 nm, respectively. Fluorescence emission were recorded at 530 nm and 590 nm for JC-1

6 monomers and JC-1 aggregates, respectively. Image processing was done using ZEN software.

7 **4.12. Protein extraction and Western blot analysis.** Cellular proteins were extracted by the

8 Column Tissue and Cell Protein Extraction Kit and the expression level of apoptosis proteins

9 was analyzed by western blot. Briefly, the A375 cells were seeded into a 100 mm dish for 24 h,

10 subjected to different treatments (12.5 µM Pal-N-Ter-TAT, pFL-N-Ter-TAT or Pal-pFL-N-Ter-

11 TAT peptide) for 24 h. The cells were washed twice with cold PBS, added denature lysate (250

12 µL) supplemented with protease inhibitor, collected into the cold purification column sleeve,

13 centrifuged at 16000 rpm for 30 s and immediately placed the collection tube on ice. Total

14 proteins were extracted successfully. The total protein content was determined by the Instant

15 BCA Protein Assay Kit. Electrophoresis with samples (20 µg/lane) was done on a 4-20% SDS

16 polyacrylamide gel. Then, they were transferred to a PVDF membrane, and were incubated

17 overnight with rabbit anti-human caspase 3, caspase 9 pAb or β-actin mAb, followed by

18 incubation for 30 min with HRP-conjugated goat anti-rabbit IgG Ab. Samples were then

19 visualized using Bio-Rad ChemiDoc MP imaging System (Bio-Rad, USA).

20

21 **Corresponding Authors**

22 Aihua Zou - [a]Shanghai Key Laboratory of Functional Materials Chemistry, School of Chemistry

23 and Molecular Engineering, East China University of Science and Technology, Shanghai 200237,

P. R. China, E-mail: aihuazou@shnu.edu.cn; [b]College of Chemistry and Materials Science, Shanghai Normal University, Shanghai 200234, P. R. China

Na Li - National Facility for Protein Science in Shanghai, Shanghai Advanced Research Institute (Zhangjiang Laboratory), Chinese Academy of Sciences, 333 Haike Road, Shanghai 201210, China, E-mail: nli@sibcb.ac.cn

Author Contributions

F. Zhang, A. Angelova, A. Zou and N. Li designed the study; F. Zhang performed the experiments; F. Zhang, A. Angelova, A. Zou and N. Li analyzed the data; V. M. Garamus did ellipsoids of rotation simulation and SAXS analysis; B. Angelov did molecular dynamic simulation and SAXS analysis; S. Tu guided immunofluorescence and WB experiments; L. Kong performed the cryo-TEM experiment; X, Zhang helped with biological experiments; F. Zhang, A. Angelova, V. M. Garamus, B. Angelov, A. Zou and N. Li wrote the manuscript.

Notes

The authors declare no conflicts of interest.

6

7 **REFERENCES**

8   (1) Hou, X.-S.; Wang, H.-S.; Mugaka, B. P.; Yang, G.-J.; Ding, Y. Mitochondria: Promising

9 Organelle Targets for Cancer Diagnosis and Treatment. *Biomater. Sci*. **2018**, *6*, 2786-2797.

10   (2) Santa-Gonzalez, G. A.; Patino-Gonzalez, E.; Manrique-Moreno, M. Synthetic Peptide

11 ΔM4-Induced Cell Death Associated with Cytoplasmic Membrane Disruption, Mitochondrial

12 Dysfunction and Cell Cycle Arrest in Human Melanoma Cells. *Molecules* **2020**, *25*, 5684-5698.

13   (3) He, S.-F.; Pan, N.-L.; Chen, B.-B.; Liao, J.-X.; Huang, M.-Y.; Qiu, H.-J.; Jiang, D.-C.;

14 Wang, J.-J.; Chen, J.-X.; Sun, J. Mitochondria-targeted Re(I) Complexes Bearing Guanidinium

15 as Ligands and Their Anticancer Activity. *J. Biol. Inorg. Chem*. **2020**, *25*, 1107-1116.

16   (4) He, Y.; Fang, X.; Shi, J.; Li, X.; Xie, M.; Liu, X. Apigenin Attenuates Pulmonary

17 Hypertension by Inducing Mitochondria-dependent Apoptosis of PASMCs via Inhibiting the

18 Hypoxia Inducible Factor 1α-KV1.5 Channel Pathway. *Chem. Biol. Interact*. **2020**, *317*, 108942-

19 108953.

1   (5) Luo, S.; Tan, X.; Fang, S.; Wang, Y.; Liu, T.; Wang, X.; Yuan, Y.; Sun, H.; Qi, Q.; Shi, C.

2   Mitochondria-targeted Small-molecule Fluorophores for Dual Modal Cancer Phototherapy. *Adv.*

3   *Funct. Mater*. **2016**, *26*, 2826-2835.

4   (6) Fulda, S. Shifting the Balance of Mitochondrial Apoptosis: Therapeutic Perspectives.

5   *Front. Oncol*. **2012**, *2*, 121-124.

6   (7) Aly, H. A. A.; Eid, B. G. Cisplatin Induced Testicular Damage Through Mitochondria

7   Mediated Apoptosis, Inflammation and Oxidative Stress in Rats: Impact of Resveratrol. *Endocr.*

8   *J*. **2020**, *67*, 969-980.

9   (8) No, M.-H.; Choi, Y.; Cho, J.; Heo, J.-W.; Cho, E.-J.; Park, D.-H.; Kang, J.-H.; Kim, C.-J.;

10   Seo, D. Y.; Han, J.; Kwak, H.-B. Aging Promotes Mitochondria-mediated Apoptosis in Rat

11   Hearts. *Life (Basel)* **2020**, *10*, 178-187.

12   (9) Shan, S.; Liu, K.; Peng, J.; Yao, H.; Li, Y.; Hong, H. Mitochondria Are Involved in

13   Apoptosis Induced by Ultraviolet Radiation in Lepidopteran Spodoptera Litura Cell Line. *Insect*

14   *Sci*. **2009**, *16*, 485-491.

15   (10) Zhao, Y.; Jiang, W.-J.; Ma, L.; Lin, Y.; Wang, X.-B. Voltage-dependent Anion Channels

16   Mediated Apoptosis in Refractory Epilepsy. *Open Medicine* **2020**, *15*, 745-753.

17   (11) Besbes, S.; Mirshahi, M.; Pocard, M.; Billard, C. New Dimension in Therapeutic

18   Targeting of BCL-2 Family Proteins. *Oncotarget* **2015**, *6*, 12862-12871.

19   (12) Han, B.; Park, D.; Li, R.; Xie, M.; Owonikoko, T. K.; Zhang, G.; Sica, G. L.; Ding, C.;

20   Zhou, J.; Magis, A. T.; Chen, Z. G.; Shin, D. M.; Ramalingam, S. S.; Khuri, F. R.; Curran, W. J.;

Deng, X. Small-molecule Bcl2 BH4 Antagonist for Lung Cancer Therapy. *Cancer Cell* **2015**, *27*, 852-863.

(13) Kang, M. H.; Reynolds, C. P. Bcl-2 Inhibitors: Targeting Mitochondrial Apoptotic Pathways in Cancer Therapy. *Clin. Cancer Res.* **2009**, *15*, 1126-1132.

(14) Arzoine, L.; Zilberberg, N.; Ben-Romano, R.; Shoshan-Barmatz, V. Voltage-dependent Anion Channel 1-based Peptides Interact with Hexokinase to Prevent Its Anti-apoptotic Activity. *J. Biol. Chem.* **2009**, *284*, 3946-3955.

(15) Liu, D.; Angelova, A.; Liu, J.; Garamus, V. M.; Angelov, B.; Zhang, X.; Li, Y.; Feger, G.; Li, N.; Zou, A. Self-assembly of Mitochondria-specific Peptide Amphiphiles Amplifying Lung Cancer Cell Death Through Targeting the VDAC1-hexokinase-II Complex. *J. Mater. Chem. B* **2019**, *7*, 4706-4716.

(16) Woldetsadik, A. D.; Vogel, M. C.; Rabeh, W. M.; Magzoub, M. Hexokinase II-derived Cell-penetrating Peptide Targets Mitochondria and Triggers Apoptosis in Cancer Cells. *Faseb J.* **2017,** *31*, 2168-2184.

(17) Amsalem, Z.; Arif, T.; Shteinfer-Kuzmine, A.; Chalifa-Caspi, V.; Shoshan-Barmatz, V. The Mitochondrial Protein VDAC1 at the Crossroads of Cancer Cell Metabolism: The Epigenetic Link. *Cancers (Basel)* **2020**, *12*, 1031-1055.

(18) Pittala, S.; Krelin, Y.; Shoshan-Barmatz, V. Targeting Liver Cancer and Associated Pathologies in Mice with a Mitochondrial VDAC1-Based Peptide. *Neoplasia* **2018**, *20*, 594-609.

1 (19) Shteinfer-Kuzmine, A.; Arif, T.; Krelin, Y.; Tripathi, S. S.; Paul, A.; Shoshan-Barmatz, V.

2 Mitochondrial VDAC1-based Peptides: Attacking Oncogenic Properties in Glioblastoma.

3 *Oncotarget* **2017**, *8*, 31329-31346.

4 (20) Liu, L.; Fang, R.; Wei, Z.; Wu, J.; Li, X.; Li, W. Giardia Duodenalis Induces Apoptosis in

5 Intestinal Epithelial Cells via Reactive Oxygen Species-mediated Mitochondrial Pathway In

6 Vitro. *Pathogens* **2020**, *9*, 693-706.

7 (21) Zhao, X.; Ren, X.; Zhu, R.; Luo, Z.; Ren, B. Zinc Oxide Nanoparticles Induce Oxidative

8 DNA Damage and ROS-triggered Mitochondria-mediated Apoptosis in Zebrafish Embryos.

9 *Aquat. Toxicol.* **2016**, *180*, 56-70.

10 (22) Malik, C.; Ghosh, S. Modulation of the Mitochondrial Voltage-dependent Anion Channel

11 (VDAC) by Hydrogen Peroxide and Its Recovery by Curcumin. *Eur. Biophys. J.* **2020**, *49*, 661-

12 672.

13 (23) Shoshan-Barmatz, V.; Shteinfer-Kuzmine, A.; Verma, A. VDAC1 at the Intersection of

14 Cell Metabolism, Apoptosis, and Diseases. *Biomolecules* **2020**, *10*, 1485-1524.

15 (24) Shoshan-Barmatz, V.; Krelin, Y.; Shteinfer-Kuzmine, A.; Arif, T. VDAC1 Functions in

16 Ca^{2+} Homeostasis and Cell Life and Death in Health and Disease. *Cell Calcium* **2018**, *69*, 81-

17 100.

18 (25) Geula, S.; Ben-Hail, D.; and Shoshan-Barmatz, V. Structure-based Analysis of VDAC1:

19 N-terminus Location, Translocation, Channel Gating and Association with Anti-apoptotic

20 Proteins. *Biochem. J.* **2012**, *444*, 475-485.

1 (26) Shi, Y.; Chen, J.; Weng, C.; Chen, R.; Zheng Y.; Chen Q.; Tang, H. Identification of the

2 Protein-protein Contact Site and Interaction Mode of Human VDAC1 with Bcl-2 Family

3 Proteins. *Biochem. Biophys. Res. Commun.* **2003**, *305*, 989-996.

4 (27) Shoshan-Barmatz, V.; Ben-Hail, D.; Admoni, L.; Krelin, Y.; Tripathi, S. S. The

5 Mitochondrial Voltage-dependent Anion Channel 1 in Tumor Cells. *Biochim. Biophys. Acta*.

6 **2015**, *1848*, 2547-2575.

7 (28) Gao, C.; Yan, X.; Wang, B.; Yu, L.; Han, J.; Li, D.; Zheng, Q. Jolkinolide B Induces

8 Apoptosis and Inhibits Tumor Growth in Mouse Melanoma B16F10 Cells by Altering

9 Glycolysis. *Sci. Rep*. **2016**, *6*, 36114-36123.

10 (29) Kudryavtseva, A. V.; Fedorova, M. S.; Zhavoronkov, A.; Moskalev, A. A.; Zasedatelev,

11 A. S.; Dmitriev, A. A.; Sadritdinova, A. F.; Karpova, I. Y.; Nyushko, K. M.; Kalinin, D. V.;

12 Volchenko, N. N.; Melnikova, N. V.; Klimina, K. M.; Sidorov, D. V.; Popov, A. Y.; Nasedkina,

13 T. V.; Kaprin, A. D.; Alekseev, B. Y.; Krasnov, G. S.; Snezhkina, A. V. Effect of Lentivirus-

14 mediated ShRNA Inactivation of HK1, HK2, and HK3 Genes in Colorectal Cancer and

15 Melanoma Cells. *BMC. Genet*. **2016**, *17*, 156-164.

16 (30) Wilson, J. E. Isozymes of Mammalian Hexokinase: Structure, Subcellular Localization

17 and Metabolic Function. *J. Exp. Biol*. **2003**, *206*, 2049-2057.

18 (31) Arbel, N.; Shoshan-Barmatz, V. Voltage-dependent Anion Channel 1-based Peptides

19 Interact with Bcl-2 to Prevent Antiapoptotic Activity. *J. Biol. Chem*. **2010**, *285*, 6053-6062.

1   (32) Hingst, J. R.; Bjerre, R. D.; Wojtaszewski, J. F. P.; Jensen, J. Rapid Radiochemical Filter

2   Paper Assay for Determination of Hexokinase Activity and Affinity for Glucose-6-phosphate. *J.*

3   *Appl. Physiol.* **2019**, *127*, 661-667.

4   (33) Sen, S.; Kaminiski, R.; Deshmane, S.; Langford, D.; Khalili, K.; Amini, S.; Datta, P. K.

5   Role of Hexokinase-1 in the Survival of HIV-1-infected Macrophages. *Cell Cycle* **2015**, *14*, 980-

6   989.

7   (34) Penso, J.; Beitner, R. Clotrimazole and Bifonazole Detach Hexokinase from Mitochondria

8   of Melanoma Cells. *Eur. J. Pharmacol.* **1998**, *342*, 113-117.

9   (35) Shteinfer-Kuzmine, A.; Amsalem, Z.; Arif, T.; Zooravlov, A.; Shoshan-Barmatz, V.

10   Selective Induction of Cancer Cell Death by VDAC1-based Peptides and Their Potential Use in

11   Cancer Therapy. *Mol. Oncol.* **2018**, *12*, 1077-1103.

12   (36) Kim, J.-M.; Jang, S.-J.; Yang, M.-H.; Cho, H.-J.; Lee, K.-H. Characterization of

13   Antibacterial Activity and Synergistic Effect of Cationic Antibacterial Peptide-resin Conjugates.

14   *B. Korean Chem. Soc.* **2011**, *32*, 3928-3932.

15   (37) Fardpour, M.; Safari, A.; Javanshir, S. γ-aminobutyric Acid and Collagen Peptides as

16   Recyclable Bifunctional Biocatalysts for the Solvent-free One-pot Synthesis of 2-

17   aminobenzothiazolomethyl-2-naphthols. *Green Chem. Lett. and Rev.* **2018**, *11*, 429-438.

18   (38) Filippova, I. Y.; Bacheva, A. V.; Baibak, O. V.; Plieva, F. M.; Lysogorskaya, E. N.;

19   Oksenoit, E. S.; Lozinsky, V. I. Proteinases Immobilized on Poly(vinyl alcohol) Cryogel: Novel

20   Biocatalysts for Peptide Synthesis in Organic Media. *Russ. Chem. B+.* **2001**, *50*, 1896-1902.

(39) Gunther, R.; Stein, A.; Bordusa, F. Investigations on the Enzyme Specificity of Clostripain: a New Efficient Biocatalyst for the Synthesis of Peptide Isosteres. *J. Org. Chem.* **2000**, *65*, 1672-1679.

(40) Fan, R.; Mei, L.; Gao, X.; Wang, Y.; Xiang, M.; Zheng, Y.; Tong, A.; Zhang, X.; Han, B.; Zhou, L.; Mi, P.; You, C.; Qian, Z.; Wei, Y.; Guo, G. Self-assembled Bifunctional Peptide as Effective Drug Delivery Vector with Powerful Antitumor Activity. *Adv. Sci.* **2017**, *4*, 1600285-1600296.

(41) Chen, X.; Chi, Y.; Bloecher, A.; Aebersold, R.; Clurman, B. E.; Roberts, J. M. N-acetylation and Ubiquitin-independent Proteasomal Degradation of p21(Cip1). *Mol. Cell* **2004**, *16*, 839-847.

(42) Skropeta, D.; Jolliffe, K. A.; Turner, P. Pseudoprolines as Removable Turn Inducers: Tools for the Cyclization of Small Peptides. *J. Org. Chem.* **2004**, *69*, 8804-8809.

(43) Zhang, X.; Li, F.; Lu, X. W.; Liu, C. F. Protein C-terminal Modification Through Thioacid/Azide Amidation. *Bioconjug. Chem.* **2009**, *20*, 197-200.

(44) Zhang, Y.; Zhang, Q.; Wong, C. T. T.; Li, X. Chemoselective Peptide Cyclization and Bicyclization Directly on Unprotected Peptides. *J. Am. Chem. Soc.* **2019**, *141*, 12274-12279.

(45) Angelov, B.; Angelova, A.; Filippov, S. K.; Drechsler, M.; Stepanek, P.; Lesieur, S. Multicompartment Lipid Cubic Nanoparticles with High Protein Upload: Millisecond Dynamics of Formation. *ACS Nano* **2014**, *8*, 5216-5226.

(46) Jeena, M. T.; Palanikumar, L.; Go, E. M.; Kim, I.; Kang, M. G.; Lee, S.; Park, S.; Choi, H.; Kim, C.; Jin, S. M.; Bae, S. C.; Rhee, H. W.; Lee, E.; Kwak, S. K.; Ryu, J.-H. Mitochondria

Localization Induced Self-assembly of Peptide Amphiphiles for Cellular Dysfunction. *Nat. Commun*. **2017**, *8*, 26-35.

(47) Corradi, E.; Meille, S. V.; Messina, M. T.; Metrangolo, P.; Resnati, G.; Halogen Bonding versus Hydrogen Bonding in Driving Self-Assembly Processes. *Angew. Chem. Int. Edit.* **2000**, *39*, 1782-1786.

(48) Nishikawa, T.; Narita, H.; Ogi, S.; Sato, Y.; Yamaguchi, S. Hydrophobicity and CH/pi-interaction-driven Self-assembly of Amphiphilic Aromatic Hydrocarbons into Nanosheets. *Chem. Commun.* **2019**, *55*, 14950-14953.

(49) Li, Y.; Angelova, A.; Hu, F.; Garamus, V. M.; Peng, C.; Li, N.; Liu, J.; Liu, D.; Zou, A. pH Responsiveness of Hexosomes and Cubosomes for Combined Delivery of Brucea Javanica Oil and Doxorubicin. *Langmuir* **2019**, *35*, 14532-14542.

(50) Fatouros, D. G.; Lamprou, D. A.; Urquhart, A. J.; Yannopoulos, S. N.; Vizirianakis, I. S.; Zhang, S.; Koutsopoulos, S. Lipid-like Self-assembling Peptide Nanovesicles for Drug Delivery. *ACS Appl. Mater. Inter.* **2014**, *6*, 8184-8189.

(51) Hamley, I. W.; Peptide Nanotubes. *Angew. Chem. Int. Ed.* **2014**, *53*, 6866-6881.

(52) Li, X.; Li, J.; Hao, S.; Han, A.; Yang, Y.; Luo, X.; Fang, G.; Liu, J.; Wang, S. Enzyme Mimics Based on Self-assembled Peptides for Di(2-ethylhexyl)phthalate Degradation. *J. Mater. Chem. B* **2020**, *8*, 9601-9609.

(53) Naskar, J.; Banerjee, A. Concentration Dependent Transformation of Oligopeptide Based Nanovesicles to Nanotubes and an Application of Nanovesicles. *Chem. Asian. J.* **2009**, *4*, 1817-1823.
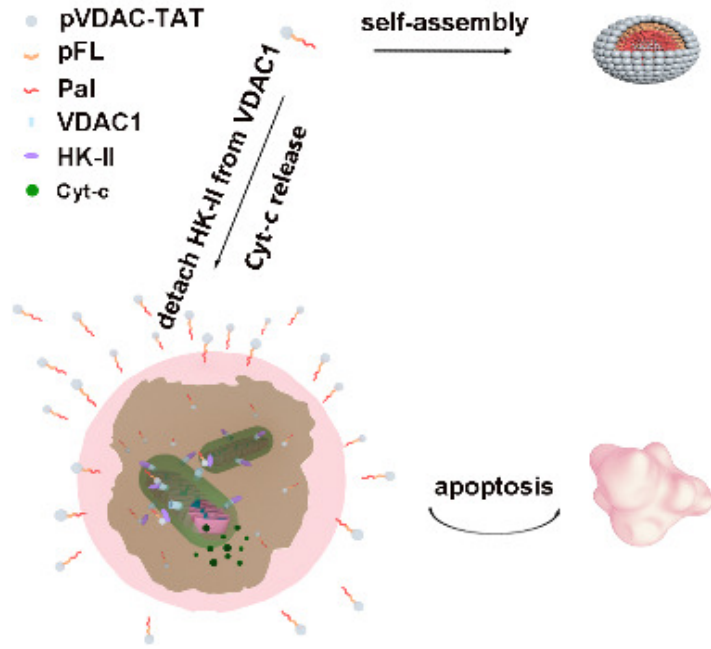
(54) Svergun, D. I. Restoring Low Resolution Structure of Biological Macromolecules from Solution Scattering Using Simulated Annealing. *Biophys. J.* **1999**, *76*, 2879-2886.

(55) Yang, W.; Chen, Y.; Zhou, X.; Gu, Y.; Qian, W.; Zhang, F.; Han, W.; Lu, T.; Tang, W. Design, Synthesis and Biological Evaluation of Bis-aryl Ureas and Amides Based on 2-amino-3-purinylpyridine Scaffold as DFG-out B-Raf Kinase Inhibitors. *Eur. J. Med. Chem.* **2015**, *89*, 581-596.

(56) Geula, S., D. Ben-Hail, and V. Shoshan-Barmatz, Structure-based analysis of VDAC1: N-terminus location, translocation, channel gating and association with anti-apoptotic proteins. Biochem J, 2012. 444(3), p. 475-85.

(57) Abu-Hamad, S., et al., The VDAC1 N-terminus is essential both for apoptosis and the protective effect of anti-apoptotic proteins. J Cell Sci, 2009. 122(Pt 11): p. 1906-16.

(58) Shi, Y., et al., Identification of the protein-protein contact site and interaction mode of human VDAC1 with Bcl-2 family proteins. Biochem Biophys Res Commun, 2003. 305(4): p. 989-96.

(59) Arbel, N., D. Ben-Hail, and V. Shoshan-Barmatz, Mediation of the antiapoptotic activity of Bcl-xL protein upon interaction with VDAC1 protein. J Biol Chem, 2012. 287(27) 23152-61.

(60) Arbel, N. and V. Shoshan-Barmatz, Voltage-dependent anion channel 1-based peptides interact with Bcl-2 to prevent antiapoptotic activity. J Biol Chem, 2010. 285(9), 6053-62.

(61) Arzoine, L., et al., Voltage-dependent anion channel 1-based peptides interact with hexokinase to prevent its anti-apoptotic activity. J Biol Chem, 2009. 284(6): p. 3946-55.

41

1   (62) Shteinfer-Kuzmine, A., et al., Selective induction of cancer cell death by VDAC1-based

2   peptides and their potential use in cancer therapy. Mol Oncol, 2018. 12(7), 1077-1103.

3   (63) Keinan, N., D. Tyomkin, and V. Shoshan-Barmatz, Oligomerization of the mitochondrial

4   protein voltage-dependent anion channel is coupled to the induction of apoptosis. Mol Cell Biol,

5   2010. 30(24), 5698-709.

6   (64) Shoshan-Barmatz, V., N. Arbel, and l. Arzoine, VDAC, the voltage-dependent anion

7   channel: function, regulation & mitochondrial signaling in cell life and death. Cell Science,

8   2008. 4, 74-118.

9   (65) Shoshan-Barmatz, V., N. Keinan, and H. Zaid, Uncovering the role of VDAC in the

10   regulation of cell life and death. J Bioenerg Biomembr, 2008b. 40(3): p. 183-91.

11   (66) Zalk, R., et al., Oligomeric states of the voltage-dependent anion channel and cytochrome

12   c release from mitochondria. Biochem J, 2005. 386(Pt 1): p. 73-83.

13   (67) Shoshan-Barmatz, V., D. Mizrachi, and N. Keinan, Oligomerization of the mitochondrial

14   protein VDAC1: from structure to function and cancer therapy. Prog Mol Biol Transl Sci, 2013.

15   117, 303-34.

16   (68) Keinan, N., et al., The role of calcium in VDAC1 oligomerization and

17   mitochondriamediated apoptosis. Biochim Biophys Acta, 2013. 1833(7), 1745-54.

18

19

20

1 **Table of Contents (TOC)**

2

pVDAC-TAT
pFL
PaI
VDAC1
HK-II
Cyt-c

detach HK-II from VDAC1

Cyt-c release

self-assembly

apoptosis

3

4